

RESEARCH ARTICLE

# 3D-bioprinted human lipoaspirate-derived cell-laden skin constructs for healing of full-thickness skin defects

Dequan Zhang<sup>1,2</sup>, Qiang Fu<sup>1</sup>, Huijuan Fu<sup>1</sup>, Jinshi Zeng<sup>3</sup>, Litao Jia<sup>3</sup>,  
Minliang Chen<sup>1\*</sup>

<sup>1</sup>Senior Department of Burns and Plastic Surgery, the Fourth Medical Center of PLA General Hospital, Beijing, 100048, China

<sup>2</sup>Central Medical Branch of PLA General Hospital, Beijing, 100120, China

<sup>3</sup>Research Center of Plastic Surgery Hospital, Chinese Academy of Medical Sciences and Peking Union Medical College, Beijing, 100144, China

## Abstract

Three-dimensional (3D)-printed bioactive scaffolds that can be produced rapidly could offer an individualized approach for treating full-thickness skin defects. Decellularized extracellular matrix (dECM) and mesenchymal stem cells have been proven to support wound healing. Adipose tissues obtained by liposuction are rich in adipose-derived dECM (adECM) and adipose-derived stem cells (ADSCs) and thus represent a natural source of bioactive materials for 3D bioprinting. Herein, ADSC-laden 3D-printed bioactive scaffolds consisting of gelatin methacryloyl (GelMA), hyaluronic acid methacryloyl (HAMA), and adECM were fabricated with dual properties of photocrosslinking *in vitro* and thermosensitive crosslinking *in vivo*. adECM was prepared by decellularization of human lipoaspirate and mixed as a bioactive material with GelMA and HAMA to form a bioink. Compared with the GelMA–HAMA bioink, the adECM–GelMA–HAMA bioink had better wettability, degradability, and cytocompatibility. Full-thickness skin defect healing in a nude mouse model showed that ADSC-laden adECM–GelMA–HAMA scaffolds accelerated wound healing by promoting faster neovascularization, collagen secretion, and remodeling. ADSCs and adECM collectively conferred bioactivity on the prepared bioink. This study represents a novel approach to enhancing the biological activity of 3D-bioprinted skin substitutes by adding adECM and ADSCs derived from human lipoaspirate and may provide a promising therapeutic option for full-thickness skin defects.

**Keywords:** Lipoaspirate; Adipose-derived stem cells; Adipose-derived decellularized extracellular matrix; 3D bioprinting; Full-thickness skin defect; Wound healing

### \*Corresponding author:

Minliang Chen  
(Chenml@sohu.com)

**Citation:** Zhang D, Fu Q, Fu H, *et al.*, 2023, 3D-bioprinted human lipoaspirate-derived cell-laden skin constructs for healing of full-thickness skin defects. *Int J Bioprint.* <https://doi.org/10.18063/ijb.718>

**Received:** December 20, 2022

**Accepted:** February 07, 2023

**Published Online:** March 23, 2023

**Copyright:** © 2023 Author(s).

This is an Open Access article distributed under the terms of the Creative Commons Attribution License, permitting distribution and reproduction in any medium, provided the original work is properly cited.

**Publisher's Note:** Whioce Publishing remains neutral with regard to jurisdictional claims in published maps and institutional affiliations.

## 1. Introduction

In China, the treatment and nursing of cutaneous wounds create a heavy burden on individuals, families, and society<sup>[1]</sup>. According to studies conducted in the USA, medical expenses incurred by repairing various wounds, particularly surgical wounds and diabetic

foot wounds, have become a substantial social burden<sup>[2]</sup>. Recently, with remarkable progress in regenerative medicine related to wound healing, skin tissue engineering has spawned the emergence of skin replacement products for wound repair. However, in a 2016 global survey of 111 specialists, 100% of the participants believed that an ideal skin substitute had yet to be developed<sup>[3]</sup>. This is due to many factors, such as the material source, preparation time, storage time, medical expense, physiological function, structure reproduction, and biological stability of previously developed tissue-engineered skin<sup>[4-7]</sup>.

Recently, many tissue engineering studies have fabricated three-dimensional (3D)-bioprinted, structurally complex scaffolds<sup>[8-10]</sup>. 3D-bioprinted structures containing pigments, or sweat glands and hair follicles have been successfully constructed *in vitro*<sup>[11,12]</sup>. The emergence of these constructs is very encouraging, but their long *in vitro* culture time may not provide patient satisfaction within a short period of time. By integrating *in situ* bioprinting system with image processing technology, autologous or allogeneic dermal fibroblasts and epidermal keratinocytes can be delivered precisely to the skin defect area, which can accelerate wound healing *in vivo*<sup>[13]</sup>. Jorgensen *et al.* produced three-layer, bioprinted skin model that encapsulated cells from a wider array of cell types, such as human keratinocytes, melanocytes, fibroblasts, dermal microvascular endothelial cells, hair follicle dermal papilla cells, and adipocytes<sup>[14]</sup>. There is no doubt that the composition or function of the newly emerging full-thickness skin constructs are increasingly similar to that of natural skin, but we should also note that most *in vitro* fabricated 3D-bioprinting scaffold require a remarkable amount of time to complete material and cell culture preparation. Confronted with urgent clinical needs, rapid fabrication of 3D-bioprinting scaffolds is essential for accelerating wound recovery and reducing scar formation<sup>[15]</sup>. There remains a lack of products using human materials and cells that can be fabricated within a few days, particularly in terms of material source and preparation time. This study will focus on this perspective.

If tissue engineering is considered an external tool, the wound microenvironment itself may serve as an internal tool to promote implant maturation. Therefore, these external and internal tools could be combined to eliminate excessive steps in *in vitro* fabrication. Therefore, rapidly fabricated 3D-bioprinted scaffolds that seem like “semifinished products” but possess biological activity could be directly implanted into the wound, where their structure and function would continue to improve depending on the wound microenvironment. We believe that this is a valuable approach, although many details regarding the wound microenvironment remain unexplored. This

treatment approach is based on the concept that if the microenvironment is regarded as a macroscopic whole, the overall regulatory direction is conducive to wound repair<sup>[16,17]</sup>. Therefore, we attempted to modify the usual strategy of *in vitro* fabrication of highly biomimetic skin substitutes by 3D bioprinting technology to a strategy of rapid *in vitro* fabrication and *in vivo* maturation in the microenvironment. Once this attempt can be realized, the preclinical time consumed by 3D bioprinting technology for wound repair will be substantially shortened.

Liposuction is a well-established procedure that is widely used in plastic surgery, and the removed fat is typically discarded as biohazardous waste<sup>[18]</sup>. This “waste” contains abundant extracellular matrix (ECM) and mesenchymal stem cells (MSCs) that fully meet the cell and material requirements for bioactive materials that support the repair of full-thickness skin defects. ECM is a natural material derived from the human body that can affect numerous cell processes, including cell spreading, growth, proliferation, migration, and differentiation, as well as organoid formation<sup>[19,20]</sup>. Decellularized ECM (dECM) does not contain cellular or nuclear components, reducing the risk of inflammatory and immune responses upon implantation, but does retain the structural and functional properties of ECM, including specific nanostructures, biochemical complexity, and bioinduction properties<sup>[21]</sup>. Importantly, dECM can promote the production of functional tissues in specific parts of the body<sup>[22]</sup>. These advantages make dECM a promising material for tissue engineering strategies for wound treatment. The thermosensitivity of dECM enables physical crosslinking at 37°C, but dECM alone is unsuitable for 3D printing because of the low viscosity<sup>[23]</sup>. Gelatin methacryloyl (GelMA) has photocrosslinking properties and can promote cell adhesion, proliferation, and spreading<sup>[24]</sup>. Hyaluronic acid methacryloyl (HAMA) has a high hydrophilicity and considerable cytocompatibility, supporting cell growth, migration, and differentiation<sup>[25]</sup>. Photocrosslinked HAMA can improve the mechanical properties of bioprinted implants. Therefore, adipose-derived decellularized extracellular matrix (adECM), together with GelMA and HAMA, as the main components of a bioink, can provide dual properties of photocrosslinking and thermosensitive crosslinking, which can further improve the stability of the scaffold after implantation.

Several studies have demonstrated the potential of adipose-derived stem cells (ADSCs) to promote wound healing<sup>[26-28]</sup>. ADSCs can differentiate into endothelial cells, fibroblasts, and keratinocytes and secrete cytokines that promote their proliferation and migration<sup>[29-32]</sup>. Biomaterial scaffolds fabricated by 3D bioprinting technology and loaded with ADSCs can promote the healing of burn

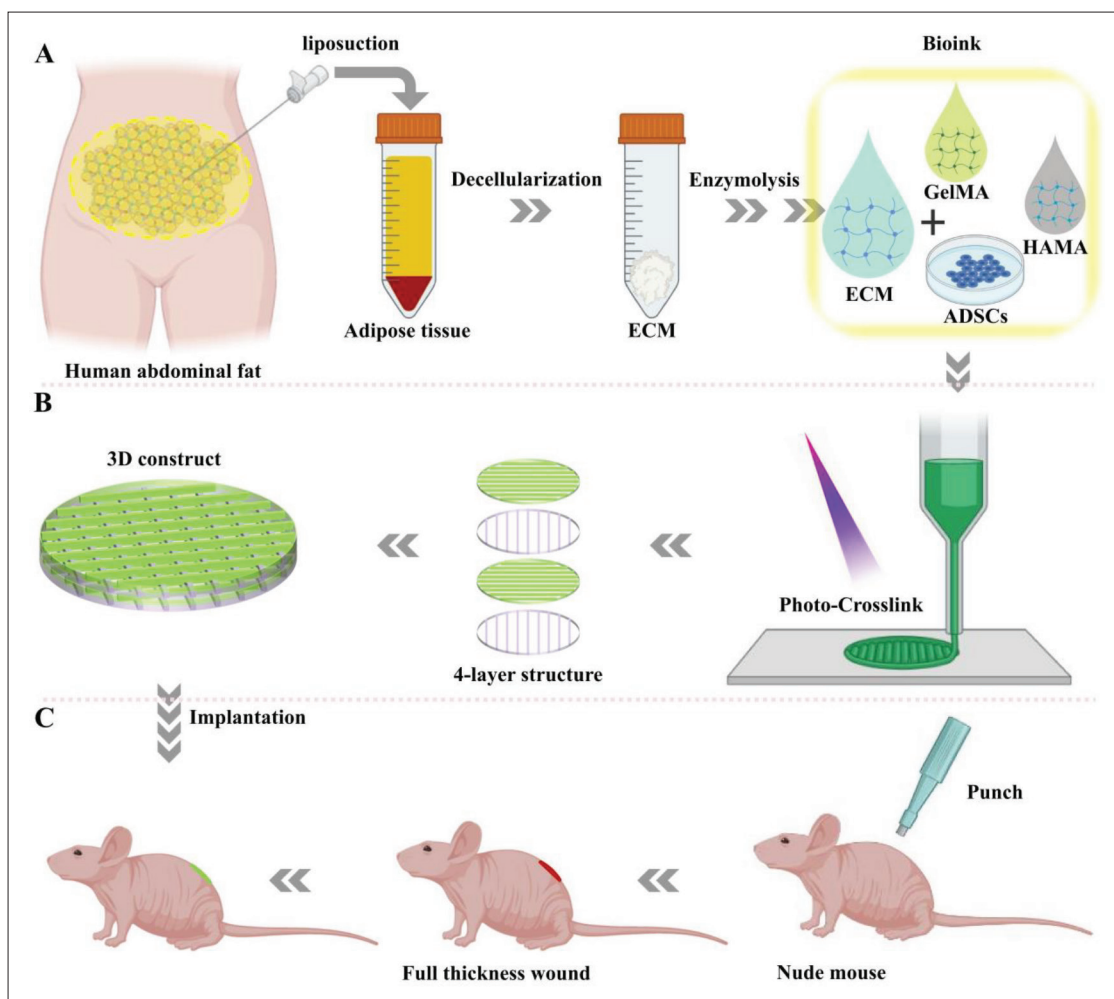


**Figure 1.** Schematic illustration of the fabrication and implantation process for ADSC-laden ECM–GelMA–HAMA constructs. (A) Human adipose tissue was decellularized, and the obtained adECM was prepared as a hydrogel. Three hydrogel materials, adECM, GelMA, and HAMA, were mixed with ADSCs at predetermined concentrations to form bioink. (B) Bioink was printed layer-by-layer, and the construction was completed by vertical superposition. (C) Constructs were implanted into the wounds of nude mice for subsequent *in vivo* studies.

wounds<sup>[33,34]</sup>. Based on the traditional concept of tissue engineering, predifferentiation of ADSCs should be completed before the printing of scaffolds; however, this approach reduces the time efficiency for clinical application. Herein, we developed a 3D-printed bioactive scaffold that can be fabricated using human adECM and ADSCs as bioink compositions and evaluated its effect on the healing of full-thickness skin defects in nude mice, thereby laying a methodological foundation for the rapid fabrication of 3D-printed skin substitutes for wound healing (Figure 1).

## 2. Materials and methods

### 2.1. Decellularization of human adipose tissue and preparation of hydrogel

Adipose tissue was harvested from the abdomen of healthy women during routine liposuction procedures at the

Senior Department of Burns and Plastic Surgery of the Fourth Medical Center of PLA General Hospital in Beijing, China (No. 2022KY135-KS001). Informed consent was obtained from the human subjects with approval from the local ethics committee of PLA General Hospital. The decellularization process followed Flynn's method<sup>[35]</sup>, with one difference involving the isopropyl alcohol extraction after the first enzymatic digestion, which was replaced every 12 h to maximize lipid removal. Reagents used for enzyme digestion included 0.25% trypsin/0.1% EDTA (Gibco, Canada), benzonase (1000 U/mL; Merck, Germany), and lipase type II (Solarbio, China). All decellularization solutions included 100 IU/mL penicillin, 100 mg/mL streptomycin, 0.625 mg/mL amphotericin (Biosharp, China), and 1% phenylmethanesulphonylfluoride (Sigma-Aldrich, USA). Collected adECM was freeze-dried in a vacuum freeze-drying machine for 48 h, and the resulting

sample was pulverized in a freeze-grinding machine. The adECM powder was then digested with 0.5 M acetic acid and 10% pepsin (Sigma-Aldrich, USA) relative to the adECM weight for 72 h. After the powder was completely dissolved, the pH of the solution was adjusted to 7.4 with 10 M NaOH, while the temperature was kept at <10°C to avoid adECM gelation. The pH-adjusted adECM hydrogel was stored at 4°C.

## 2.2. Evaluation of adipose-derived decellularized ECM

To evaluate the decellularization efficiency, residual DNA within the adECM was extracted using a genomic DNA extraction kit (Tiangen, China) and measured using the NanoDrop system (Thermo, USA). The DNA quantity was normalized to the initial dry weight of the tissue. Sircol collagen and Blyscan sGAG assay kits (Biocolor, UK) were used to evaluate the collagen and sulfated glycosaminoglycan (sGAG) content, respectively, of decellularized samples. Hematoxylin and eosin (H&E) staining was performed to visualize any remaining nuclei. An Oil Red O staining kit (Solebo, China) was used to stain residual lipids in the adECM.

## 2.3. Culture and identification of ADSCs

ADSCs were obtained from the adipose tissue of the patient undergoing liposuction as mentioned in section 2.1. Isolation and culture of ADSCs were performed as previously described<sup>[31]</sup>. Liposuction was digested with 0.1% collagenase type I (Sigma-Aldrich, USA) for 60 min at 37°C. Samples were then filtered through a 200-mesh filter. The filtrate was centrifuged at 1200 ×g for 5 min. Pelleted cells were washed and resuspended in L-DMEM (HyClone, USA) supplemented with 10% fetal bovine serum (FBS) and 1% penicillin–streptomycin–amphotericin in a humidified atmosphere of 5% CO<sub>2</sub> at 37°C. Cells from the third to fifth passages were used for experiments. Commercial kits (Cyagen, China) were used to examine the adipogenic, osteogenic, and chondrogenic differentiation abilities of the ADSCs following the manufacturer's protocols. Cells were stained with Oil Red O, Alizarin red, and Alcian blue to assess adipogenic, osteogenic, and chondrogenic differentiation, respectively. Flow cytometry (BD Biosciences, USA) was used to detect the expression of cell surface markers, such as CD31, CD34, CD45, CD73, and CD90.

## 2.4. Bioink formulation and cell encapsulation

To improve adECM hydrogel formability for 3D printing, GelMA and HAMA (SunP Biotech, China) were used as composite components of the prepared bioink herein based on their photocrosslinked properties. The final concentrations of adECM, GelMA, and HAMA in the bioink formulation were 1.125%, 7.5%, and 1% w/v,

respectively. A bioink solution of 7.5% w/v GelMA + 1% w/v HAMA without adECM was prepared. After the bioink solutions were pasteurized, a 10% volume concentration of the photoinitiator lithium phenyl-2,4,6-trimethyl benzoyl phosphinate was added. Before bioprinting, ADSCs were detached using 0.25% trypsin/0.1% EDTA. After centrifugation, cells were suspended in phosphate-buffered saline (PBS) and then mixed with the bioink at a 1:9 ratio. The final working concentration of cells was  $1.0 \times 10^7$  cells/mL in the cell-laden bioink. 3D bioprinting was performed as soon as the bioink with all components was prepared.

## 2.5. Rheological characterization of bioinks

The rheological properties of the two acellular bioinks with and without adECM were analyzed using a HR-20 hybrid rheometer (TA Instruments, USA) equipped with a 40-mm diameter parallel-plate geometry and a gap size of 1 mm. The storage ( $G'$ ) and loss modulus ( $G''$ ) were recorded at a rate of 3°C/min from 0°C to 35°C under a fixed frequency of 1 Hz and strain of 2%. The viscosity was measured in two aspects. First, the effect of temperature on the viscosity was observed at a fixed shear rate of 1 1/s from 0°C to 30°C. Then, the effect of shear rate on viscosity was recorded for a shear rate change from 0.1 to 100 1/s at 17°C. A time-sweep oscillatory test with a fixed frequency of 1 Hz, strain of 2%, and temperature of 25°C was used to record the modulus changes of the samples before and after 10 s of UV irradiation with a 405-nm UV lamp (CREE, China).

## 2.6. Swelling of photocrosslinked bioinks

Photocrosslinked samples of the two acellular bioinks with and without adECM were immersed in PBS at 37°C for the following time intervals: 1, 6, 12, and 24 h. At each timepoint, excess PBS was drained from scaffold surfaces, and the scaffold weight was then measured and recorded as  $W_1$ . Scaffolds were lyophilized for 1 week, and the weight of each after lyophilization was recorded as  $W_0$ . The swelling ratio (SR) was calculated using Equation I:

$$SR = (W_1 - W_0)/W_0 \quad (I)$$

## 2.7. Degradation of photocrosslinked bioink scaffolds

Scaffolds prepared from the two acellular bioinks were lyophilized, and initial masses were recorded as  $W_0$ . Dried scaffolds were rehydrated in PBS for 24 h and subsequently transferred to PBS containing 1.5 U/mL collagenase II for incubation with shaking at 37°C. Samples were removed at different time points for lyophilization, and the weights of dried samples were recorded as  $W_t$ . The percent of remaining mass (RM) after degradation was calculated using Equation II:

$$RM(\%) = W_t/W_0 \times 100\% \quad (II)$$



## 2.8. Scanning electron microscopy

To remove moisture from the hydrogel, acellular samples were vacuum-freeze-dried, followed by sputtering, and coated with iridium to avoid charge accumulation. Lyophilized samples were cut with a razor to expose the internal structure and placed on the sample stub, with tangent facing up. A scanning electron microscope (SEM, S-4800, HITACHI, Japan) was used to examine sample pore structures, and images were obtained with an accelerating voltage of 15 kV at a working distance of 10 mm.

## 2.9. Cytocompatibility of photocrosslinked bioinks

After crosslinking with 405-nm UV light, 200  $\mu$ L of acellular bioink samples were transferred to a 24-well plate and immersed in 2 mL Dulbecco's modified Eagle medium (DMEM)-F12 medium containing 10% FBS in a humidified atmosphere of 5% CO<sub>2</sub> at 37°C for 3 days. The samples were then removed, and the solution containing the eluent was collected. The eluent solution was supplemented with 10% FBS and 1% penicillin–streptomycin–amphotericin and stored at 4°C for later use. ADSCs ( $5 \times 10^3$  cells/well) were cultured in 96-well plates with 100  $\mu$ L of the above-mentioned eluent solution per well for 1, 3, and 7 days. The blank control group was cultured in DMEM-F12 medium containing 10% FBS and 1% penicillin–streptomycin–amphotericin. After washing with PBS, ADSCs were treated with a mixture of DMEM-F12 medium (90  $\mu$ L) and CCK-8 reagent (10  $\mu$ L) for 2 h. ADSC proliferation was determined using a CCK-8 assay (Dojindo Molecular Technologies, Japan), and the absorbance value of the sample solutions at 450 nm was measured using a microplate reader (ELX 800; BioTek Instruments, USA).

## 2.10. Fabrication of 3D-bioprinted scaffolds

Four-layer circular scaffolds were printed layer-by-layer using a commercial 3D printer (Envision TEC, Germany) by extruding bioinks with a thermo-controlled chamber at 16°C–18°C, a 27G nozzle with an inner diameter of 200  $\mu$ m, a pneumatic pressure of 0.8–1.2 bar, and a moving speed of 3.2–5.6 mm/s. Scaffolds had an 8-mm diameter with an 800- $\mu$ m strand spacing and 180- $\mu$ m layer height. Photocrosslinking was performed by irradiating the scaffolds for 3–5 s with 405-nm UV light immediately after the printing process for each layer was completed. Scaffolds were temporarily immersed in DMEM-F12 medium containing 10% FBS and maintained under normal culture conditions for later use.

## 2.11. Biocompatibility of adECM–GelMA–HAMA scaffold

A calcein-AM/propidium iodide (PI) double staining kit (Dojindo Molecular Technologies, Kumamoto, Japan) was used to assess the biocompatibility of prepared scaffolds according to the manufacturer's instructions.

Scaffolds carrying ADSCs were placed in 24-well plates, and then DMEM-F12 medium was added for culture under standard conditions at 37°C. On days 0, 3, and 7, scaffolds were collected, rinsed with PBS three times, and stained in 2-mL solution containing 2  $\mu$ mol/L calcein-AM and 4.5  $\mu$ mol/L PI at 37°C for 15 min. Fluorescent images of stained cells within scaffolds were obtained using a confocal laser scanning microscope (Leica TCS SP8, Leica, Germany). To evaluate ADSC viability at different time points, the numbers of live and dead cells were counted in the fluorescent confocal microscopy images using Image-Pro-Plus 6.0 software.

## 2.12. In vivo wound healing

All animal experiments were approved by the ethics committee of the Fourth Medical Center of the PLA General Hospital (No. 2022-X18-03). Thirty female BALB/c nude mice, aged 4–5 weeks old and weighing 19.13–22.47 g, were purchased from Beijing Vital River Laboratory Animal Technology (Beijing, China). After anesthesia, two full-thickness excisional skin wounds with 8-mm diameters were created using a trephine on the backs of nude mice. A rubber ring with an 8-mm inner diameter was sutured around the wound with 6-0 nylon to minimize wound contraction. Mice were randomly divided into five groups ( $n = 6$  per group) where wounds were filled with no treatment, ADSC-laden adECM–GelMA–HAMA, acellular adECM–GelMA–HAMA, ADSC-laden GelMA–HAMA, or acellular GelMA–HAMA. After scaffold placement, the wound was covered with a semipermeable membrane and bandaged, and mice were housed and fed in separate cages. Images of the wounds were taken at 0, 7, and 14 days, and the wound residual rate was calculated using Equation III:

$$\text{Wound residual rate} = (\text{Residual area} / \text{Original area}) \times 100\% \quad (\text{III})$$

Mice were euthanized at either day 7 or 14 after implantation for the harvesting of wound tissues, which were then processed for analysis.

## 2.13. Histological and immunohistochemical staining of wound tissues

Wound tissues harvested after 7 or 14 days were fixed in 4% paraformaldehyde, dehydrated in a graded alcohol series, and embedded in paraffin. The tissues were then sliced into 4- $\mu$ m-thick sections perpendicular to the wound surface for further staining. Each section was stained with H&E and Masson's trichrome stain. Picrosirius red staining was performed to visualize collagen fibers using a Picrosirius Red Staining Kit (Yeasen Biotechnology, China). Images were taken under polarized light with a Nikon Eclipse Ci microscope (Nikon, Tokyo, Japan). For immunohistochemical staining, deparaffinized sections were evaluated for CD31 expression using a staining kit

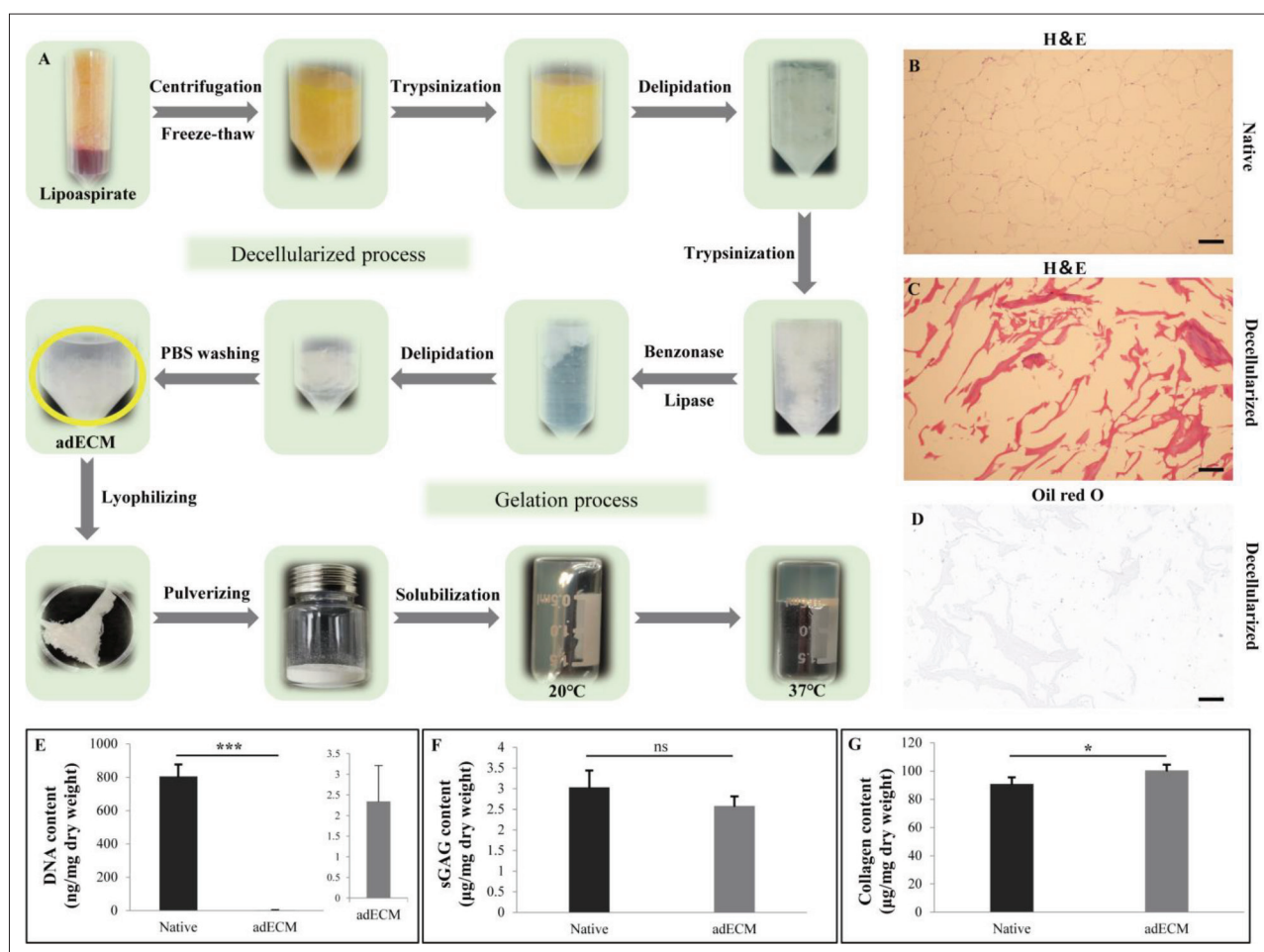


**Figure 2.** Preparation and evaluation of adECM hydrogels. (A) Main steps of adECM preparation, including the sol–gel transition with increasing temperature. (B) Representative image of H&E-stained native human adipose tissue. Scale bar: 100 μm. (C, D) Representative images of H&E- and Oil Red O-stained decellularized human adipose tissue, respectively. Scale bar: 100 μm. (E, F and G) Quantitative measurements of DNA, sGAG, and collagen content of native human adipose tissue and adECM. \* $p < 0.05$ , \*\* $p < 0.01$ , and \*\*\* $p < 0.001$ .

according to the manufacturer's instructions (Affinity Biosciences, China). Stained sections were observed using a BX51 microscope (Olympus, Japan).

## 2.14. Statistical analysis

Data are representative of at least three experiments and are presented as mean  $\pm$  standard deviation. One-way analysis of variance was used for comparisons among multiple groups, followed by Tukey's multiple comparisons test, and adjusted  $p$ -values were obtained using GraphPad Prism 9.0 software. Values of  $p < 0.05$  were indicative of significant differences.

## 3. Results and discussion

### 3.1. Preparation and characterization of adECM hydrogel

adECM hydrogel was prepared using the procedure outlined in Figure 2A. After 5 consecutive days of

decellularization, flocculent-hydrated ECM was obtained. Hydrated adECM was subsequently freeze-dried and ground into white powder, which was digested by pepsin. Upon rehydration and adjustment of the pH, adECM hydrogel was formed. The adECM hydrogel exhibited a temperature-sensitive sol–gel phase transition with solid-state characteristics at 37°C. To evaluate the decellularization effect, we performed H&E and Oil Red O staining. Adipocytes in the native adipose tissue showed an intact structure and were arranged in a network, with blue-stained nuclei clearly visible within the cells (Figure 2B). Hydrated adECM showed a lack of any blue-stained nuclei or cellular structures and only contained red-stained ECM components (Figure 2C). Oil Red O staining of adECM showed no residual red-stained lipids (Figure 2D).

Verification of residual cellular material is required and is mainly accomplished by examining the remaining DNA and genomic residues<sup>[36]</sup>. The DNA content in

adECM was 99.71% lower than that of native tissue ( $2.34 \pm 0.87$  vs.  $804.02 \pm 72.74$  ng/mg dry weight, respectively; Figure 2E) and substantially below the minimal criterion for decellularization ( $<50$  ng/mg dry weight)<sup>[37]</sup>. The sGAG content was  $2.58 \pm 0.26$  and  $3.03 \pm 0.41$   $\mu$ g/mg dry weight in adECM and native tissue, respectively, indicating that most sGAG components were retained in adECM, although the difference between them was not significant ( $p > 0.05$ ) (Figure 2F). The collagen content levels in adECM and native tissues were  $100.38 \pm 4.21$  and  $90.8 \pm 4.84$   $\mu$ g/mg dry weight, respectively (Figure 2G). The collagen content was remarkably increased in the adECM compared with that in native adipose tissue, and this may be due to the low proportion of collagen in adipose tissue, which would naturally increase with the removal of adipocytes. This is consistent with the results of Pati *et al.*, who reported that the GAG content decreased, while the collagen content increased after decellularization of adipose tissue<sup>[38]</sup>. This elevated collagen content could be an advantage for adECM as a component of bioink for a 3D-printed skin substitute.

### 3.2. Printability of bioinks

The rheological properties of hydrogels are an important basis for evaluating their printability<sup>[39]</sup>. First, the gelation kinetics of bioinks were evaluated by performing temperature sweep experiments. Both bioinks exhibited thermally sensitive properties, with the storage ( $G'$ ) and loss modulus ( $G''$ ) values changing abruptly when the temperature neared the gel point, indicating that the bioinks were changing from a liquid to a gel, which is a prerequisite for ensuring that hydrogels form after printing. The gel point is the temperature corresponding to the intersection point of  $G'$  and  $G''$ . The gelation temperature ranges of adECM–GelMA–HAMA and GelMA–HAMA were  $16.5^\circ\text{C}$  and  $17.4^\circ\text{C}$ , respectively (Figure 3A). The viscosity of both bioinks decreased with increasing temperature from  $0^\circ\text{C}$  to  $30^\circ\text{C}$  (Figure 3B). The loss tangent ( $\tan\delta = G''/G'$ ) tended to increase as the temperature increased, showing a transition from solid-like behavior ( $\tan\delta < 1$ ) to liquid-like behavior ( $\tan\delta > 1$ ; Figure 3C).

Bioinks required a viscosity that was appropriate for controllable printing with excellent shape fidelity<sup>[40]</sup>. Bioink viscosity was recorded over the shear rate range of  $0.1$ – $100$  Hz at  $17^\circ\text{C}$ . Rheological analysis showed that the viscosity of adECM–GelMA–HAMA at  $0.1$  Hz was  $82.67 \pm 6.71$  Pa·s, which decreased to  $1.62 \pm 0.13$  Pa·s at the highest shear rate of  $100$  Hz. The viscosity of GelMA–HAMA was  $110.33 \pm 5.02$  Pa·s at  $0.1$  Hz and decreased to  $1.98 \pm 0.09$  Pa·s at the highest shear rate of  $100$  Hz. Both bioinks exhibited shear-thinning properties, with the viscosity decreasing under increased shear strain (Figure 3D). Therefore, both bioinks could be smoothly

extruded through the 3D printer nozzle without blockage, making them suitable for 3D-bioprinting.

We also observed the modulus change after photocrosslinking. After  $10$  s of UV irradiation, the moduli of both bioinks increased rapidly, and the value of  $G'$  changed from being lower than that of  $G''$  before crosslinking to being much higher than that of  $G''$ . The  $G'$  value of adECM–GelMA–HAMA increased by  $>79$ -fold, whereas the value of  $G''$  increased by approximately  $11$ -fold, and the respective increases for  $G'$  and  $G''$  values for GelMA–HAMA were approximately  $72$ - and  $4$ -fold, respectively (Figure 3E and F).

These results indicate that the bioink may have acceptable printability and shape retention ability. In particular, this shape retention ability could enable the printed scaffold to more effectively fill and contact the wound microenvironment for a sufficient time throughout wound healing, thus establishing a dynamic microenvironment where cells in the scaffold interact with the wound and those surrounding the wound interact with the scaffold.

### 3.3. Physical characterization of bioinks

The water uptake capacity is an important criterion to consider because the encapsulated cells absorb nutrients from the wound to maintain their growth and proliferation<sup>[41]</sup>. For analysis of bioink scaffold swelling, the weight of hydrogel samples was measured at different time points within a  $24$  h incubation at  $37^\circ\text{C}$ . GelMA–HAMA and adECM–GelMA–HAMA samples exhibited rapid water absorption after  $1$  h of incubation, with SRs of  $3.94 \pm 0.32$  and  $4.89 \pm 0.34$ , respectively. After  $12$  h of incubation, the swelling plateaued, and by  $24$  h, the swelling ratios were  $8.95\% \pm 0.72\%$  and  $11.18\% \pm 0.45\%$ , respectively. The swelling ratio of GelMA–HAMA was remarkably lower than that of adECM–GelMA–HAMA at different time points (Figure 4A).

To analyze bioink degradation, we used collagenase treatment at several time points  $>72$  h to calculate the rate of weight loss. The RM of adECM–GelMA–HAMA was remarkably higher than that of GelMA–HAMA after the experimental time course, and approximately  $53.06\% \pm 5.16\%$  of the adECM–GelMA–HAMA mass remained at  $72$  h compared with only  $37.53\% \pm 4.52\%$  of GelMA–HAMA (Figure 4B).

SEM was performed to observe the pore structure of the two bioinks, as this property can affect cell behaviors, such as cell spreading, as well as the nutrient and oxygen supply and metabolite removal. The 3D structures of the two bioink hydrogels showed a reticular porous morphology (Figure 4C and D). The porous structure with a network distribution is an important basis for promoting the attachment and



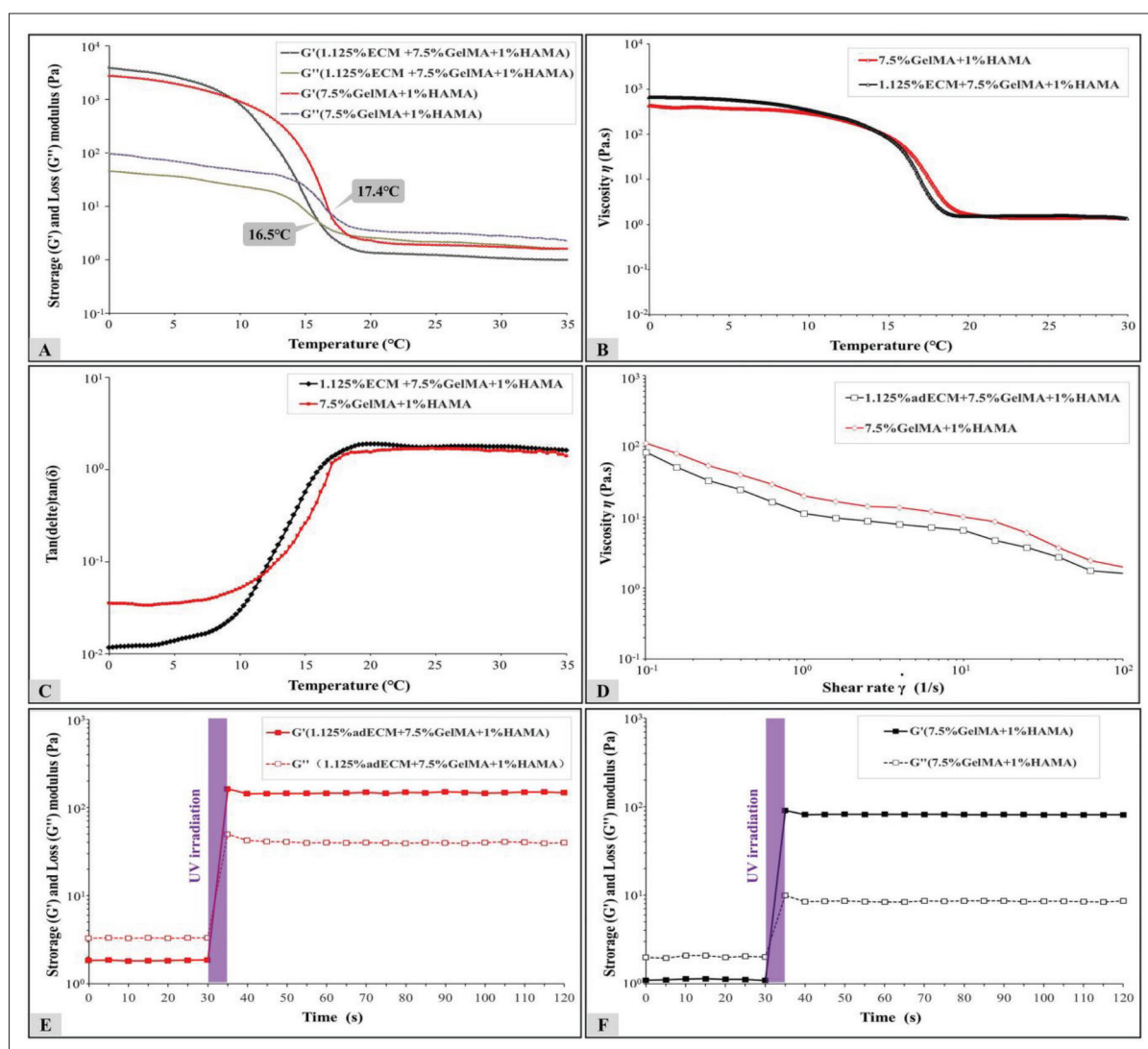


**Figure 3.** Rheological properties of bioinks with and without adECM. (A) Effect of temperature on storage modulus ( $G'$ ) and loss modulus ( $G''$ ). (B) Effect of temperature on viscosity. (C) Effect of temperature on loss tangent. (D) Effect of shear rate on viscosity at 17 °C. (E, F) Modulus changes before and after photocrosslinking.

migration of encapsulated cells<sup>[42]</sup>. In addition, attention should be paid to the pore size. An internal pore size that is too small will cause nutrient deficiency and slow cell growth, whereas a larger pore size is more suitable for cell growth, proliferation, and migration<sup>[43]</sup>. The measured pore diameters were  $131.39 \pm 6.88 \mu\text{m}$  ( $107.6 \pm 6.35$  pores per  $1 \times 1 \text{ mm}$  field on SEM) for adECM–GelMA–HAMA and  $112.16 \pm 8.07 \mu\text{m}$  ( $143 \pm 5.24$  pores per  $1 \times 1 \text{ mm}$  field on SEM) for GelMA–HAMA (Figure 4E and F). This indicates that adECM–GelMA–HAMA may be more suitable for cell growth than GelMA–HAMA.

### 3.4. Morphology and verification of ADSCs

Adherent ADSCs showed a fibroblastic morphology (Figure 5A), but under the respective inductive culture

conditions, ADSCs differentiated into adipocytes, osteoblasts, and chondroblasts based on the observation of lipid droplets by Oil Red O staining, calcium deposition by Alizarin red staining, and chondrogenic nodules by Alcian blue staining, respectively (Figure 5B). Flow cytometric analysis showed that ADSCs were positive for CD90 and CD73 expression but negative for CD31, CD34, and CD45 expression (Figure 5C). Thus, isolated cells displayed typical ADSC characteristics.

### 3.5. Bioprinting of ADSC-laden scaffolds

Generally, 3D bioprinting can be divided into three types, including vat polymerization, jetting, and extrusion-based bioprinting. Vat polymerization-based bioprinting technique produces solid objects layer-by-layer via



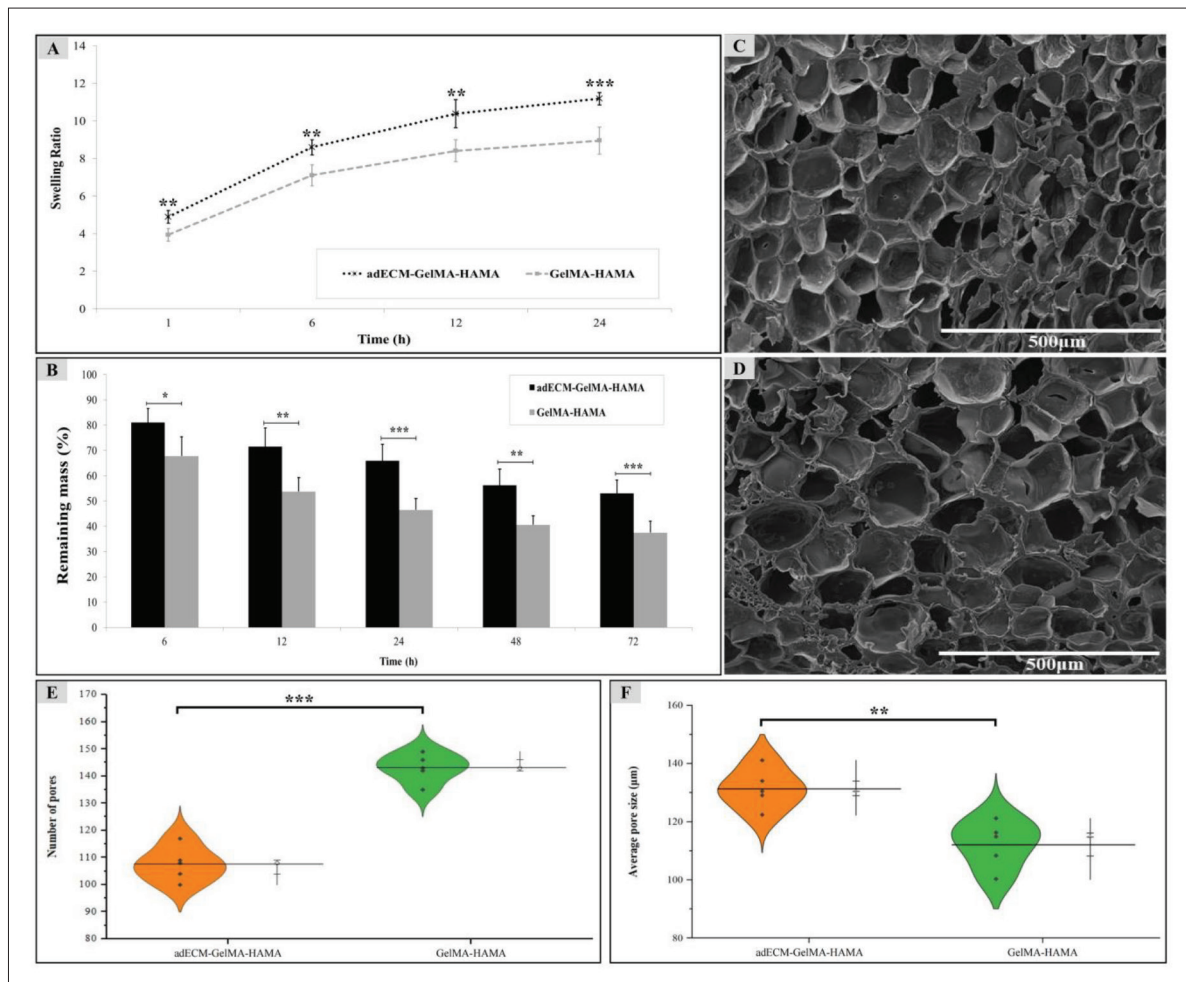


**Figure 4.** Microstructure and physicochemical properties of bioinks. (A) Swelling ratio. (B) In vitro degradation. (C) Representative SEM micrographs of GelMA-HAMA bioink. (D) Representative SEM micrographs of adECM-GelMA-HAMA bioink. (E) Number of pores per  $1 \times 1$  mm field on SEM. (F) Average diameter of pores within lyophilized hydrogels. \* $p < 0.05$ , \*\* $p < 0.01$ , and \*\*\* $p < 0.001$ .

photopolymerization of a vat of liquid resin. However, the use of single bio-resin is still a major bottleneck for its application in tissue engineering<sup>[44]</sup>. Jetting-based bioprinting enables drop-on-demand patterning of different types of cells and biomaterials in a noncontact profile, with the advantages of high throughput and efficiency. Notably, controlling the droplet volume and impact velocity during printing can improve cell viability and proliferation<sup>[45]</sup>. Extrusion-based bioprinting has become the most common bioprinting technique due to its quick production time, ease of operation, and compatibility with a variety of bioinks. Bioinks in the cartridges are extruded using either pneumatic pressure or mechanical force to the preset position through a nozzle (Figure 6A). It enables the bioprinting of bioinks with high-cell densities. The shear stress generated by high extrusion pressure during extrusion-based bioprinting may damage cells, so cell viability needs to be assessed after printing<sup>[46]</sup>. adECM

with weak mechanical properties can form composites together by materials with shear thinning properties, such as the adECM-GelMA-HAMA bioink in this study. Shear stress during extrusion can disrupt the weak interactions between the bio-macromolecular gels and force the material to flow through the nozzle. This is precisely why extrusion-based bioprinting was chosen for this study.

To evaluate bioink printability, the cartridge temperatures for adECM-GelMA-HAMA and GelMA-HAMA were  $16^{\circ}\text{C}$ – $17^{\circ}\text{C}$  and  $17^{\circ}\text{C}$ – $18^{\circ}\text{C}$ , respectively, based on the sol-gel transition temperatures determined by rheological analysis. A four-layer circular structure with an 8-mm diameter was fabricated via layer-by-layer photocrosslinking in the bioprinting process (Figure 6B and C). High-definition images showed that the scaffold structure was consistent with the design pattern and that the scaffolds had a regular porous structure (Figure 6D).

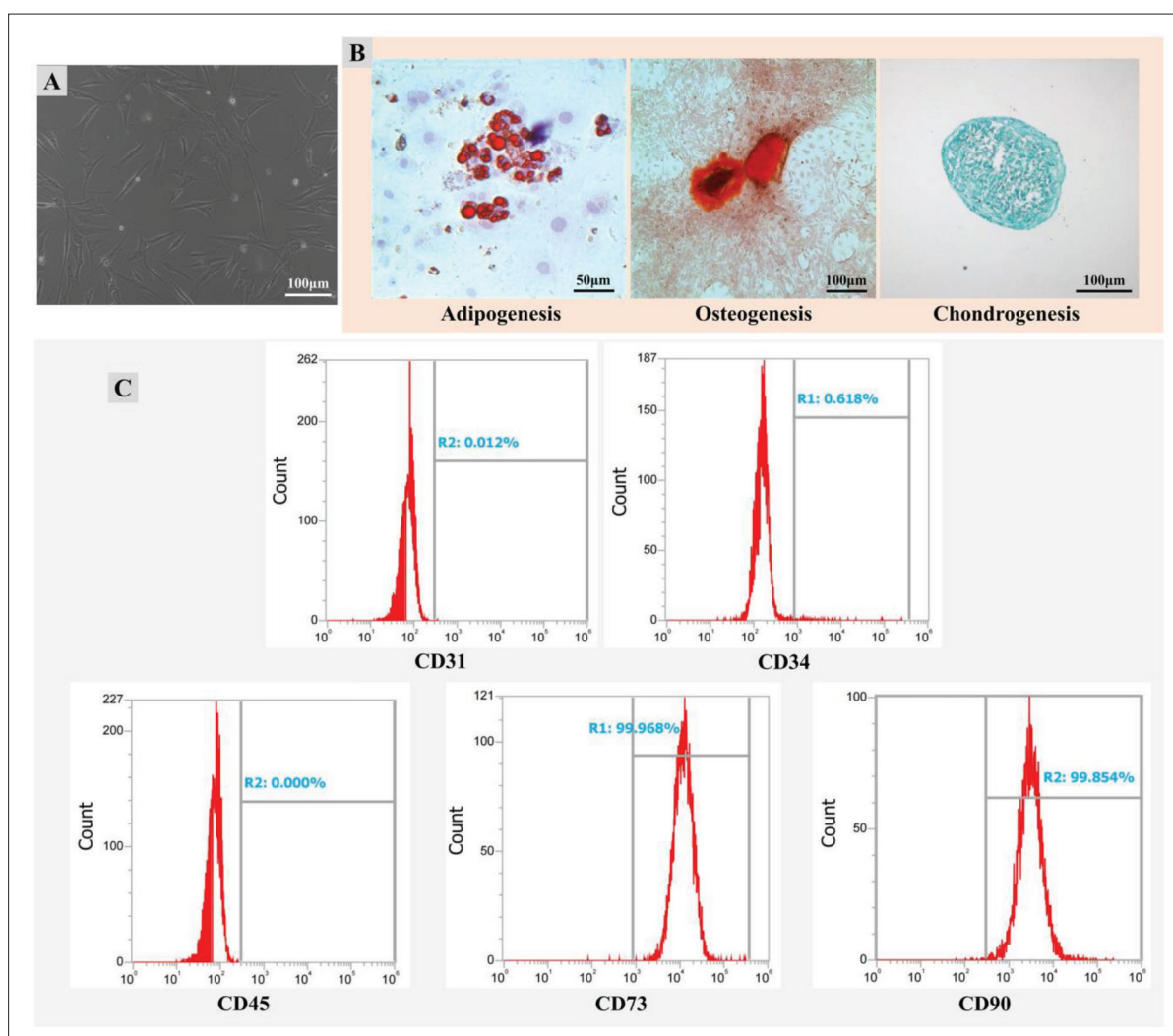


**Figure 5.** Characterization of ADSCs. (A) ADSCs showed a typical fibroblastic morphology. (B) Differentiation of ADSCs into adipocytes, osteoblasts, and chondrocytes was detected using Oil Red O, Alizarin red, and Alcian blue staining, respectively. (C) ADSCs stained positive for CD90 and CD73 expression and negative for CD31, CD34, and CD45 expression.

Light microscopy showed that the reticular structure had a nonsmooth surface, which may be more conducive to cell growth and interaction between the scaffold and the wound microenvironment (Figure 6E). SEM showed that the original structure was retained after lyophilization, although with a degree of surface shrinkage deformation (Figure 6F).

### 3.6. Biocompatibility of bioinks and 3D-printed bioink scaffolds

Cells in the scaffold with 7.5% GelMA had greater viability, proliferation, and spreading compared with those in scaffolds with 5% and 10% GelMA<sup>[47]</sup>, and the 7.5% GelMA was chosen for further study. To determine whether bioink components affect the viability of ADSCs, CCK-8 assays were performed. Based on increasing optical

density (OD) values over time, ADSCs in the mixture remained viable and proliferated, indicating that the two bioink formulations did not exhibit any biological toxicity. Notably, OD values for ADSCs loaded in adECM–GelMA–HAMA were higher than those in GelMA–HAMA at all timepoints, suggesting that adECM could improve the activity of ADSCs (Figure 7A–C). To visualize the effect of the bioprinting process and photocrosslinking on cell viability, we performed live/dead staining of ADSCs within the scaffolds at 1, 3, and 7 days after printing. Bioink-formed 3D structures were maintained for 7 days, indicating their high structural stability. The ADSCs in each scaffold type survived, and the number of live cells increased with the prolonged culture time (Figure 7D). The percentages of viable cells in the adECM–GelMA–HAMA group on days 1, 3, and 7 were  $97.24\% \pm 1.18\%$ ,

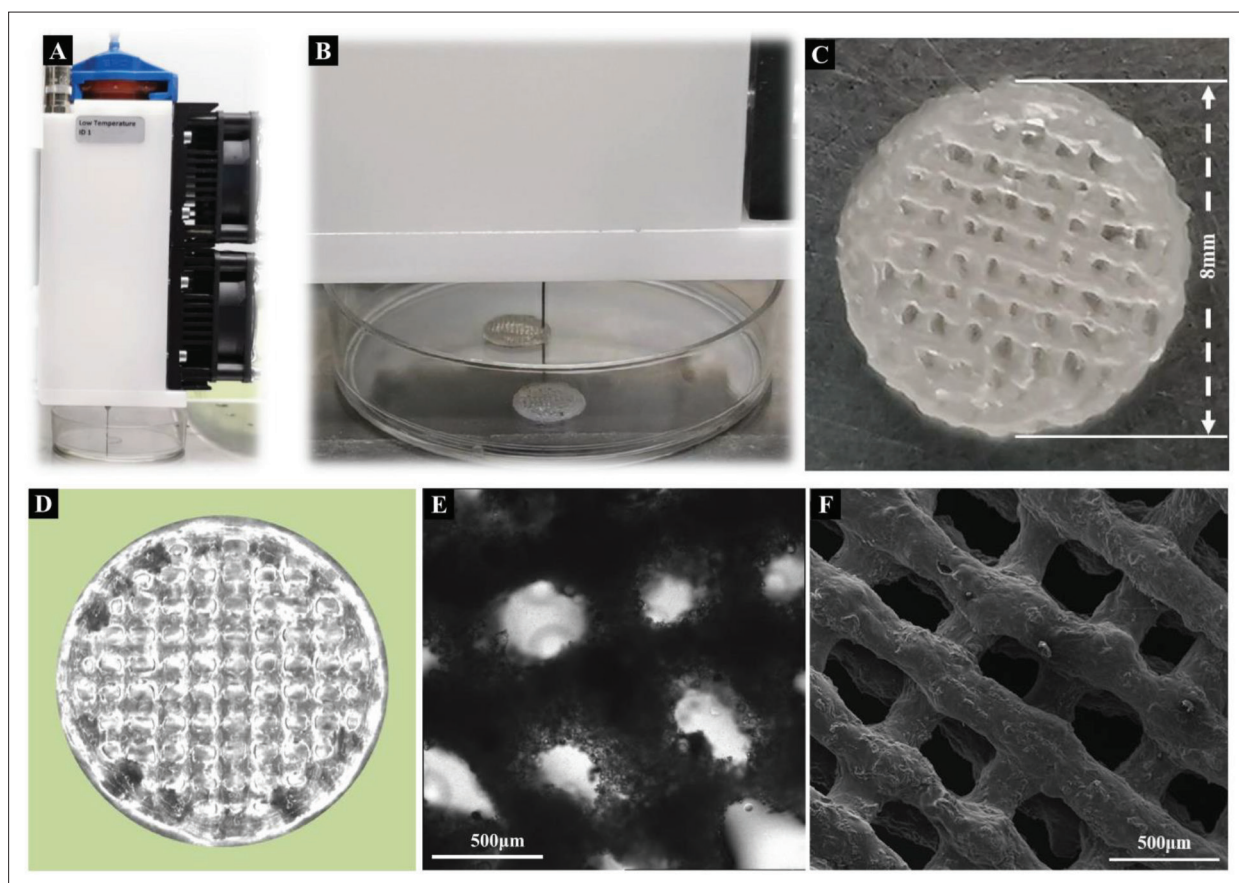


**Figure 6.** Fabrication of 3D-printed constructs. (A) 3D-bioprinting platform. (B) Bioink was used for printing in a layer-by-layer style in a sterile environment. (C) Printed constructs exhibited a complex lattice-shaped structure as expected. (D) Image taken by the printer's high-definition camera. (E) Representative microscopic image of printed construct. (F) Representative SEM micrograph of printed construct.

95.73%  $\pm$  1.21%, and 96.17%  $\pm$  1.05%, respectively, and those in the GelMA–HAMA group were 96.43%  $\pm$  1.07%, 95.35%  $\pm$  1.52%, and 95.19%  $\pm$  1.4%, respectively. No significant difference in cell viability was observed between the two bioinks (Figure 7E and F). CCK-8 assay and live/dead staining results together demonstrated the biocompatibility of adECM–GelMA–HAMA. We propose that the high cell viability in both groups may be related to the nutrient-rich medium used for cell growth *in vitro*, which differs from the complex wound microenvironment *in vivo*<sup>[17]</sup>. Although no significant difference was observed between the two bioink groups, cell viability was >95% in both groups. Together, the CCK-8 assay results and live/dead staining results demonstrated the biocompatibility of both prepared bioinks.

### 3.7. *In vivo* wound healing after treatment with 3D-bioprinted scaffolds

A full-thickness skin defect model in nude mice was used to evaluate the effectiveness of ADSC-laden 3D-bioprinted adECM–GelMA–HAMA scaffolds for promoting the wound-healing process (Figure 8A). Gross observation

of wound closure showed that the wound area decreased over time in each treatment group. However, wound sizes differed among the groups, and on day 7 after implantation, the wound area of the blank control group decreased the most slowly. On day 14, the two groups with ADSC-laden scaffolds had achieved complete wound closure. Notably, the skin in the ADSC-laden adECM–GelMA–HAMA group had healed more completely, whereas that in the ADSC-laden GelMA–HAMA group still showed an area of poor epithelization. In both treatments with acellular scaffolds, a small area of unclosed wound remained, but the wound areas in these groups were smaller than those in the blank control group (Figure 8B).

Quantitative measurement of wound closure showed that the area of the unclosed wound at day 7 was remarkably smaller in the ADSC-laden adECM–GelMA–HAMA group (15.4%  $\pm$  1.56%) than that in the ADSC-laden GelMA–HAMA, adECM–GelMA–HAMA, GelMA–HAMA, and blank control groups (26.43%  $\pm$  4.11%, 29.47%  $\pm$  3.23%, 34.68%  $\pm$  3.73%, and 54.48%  $\pm$  6.59%, respectively). On day 14, the wound area in the



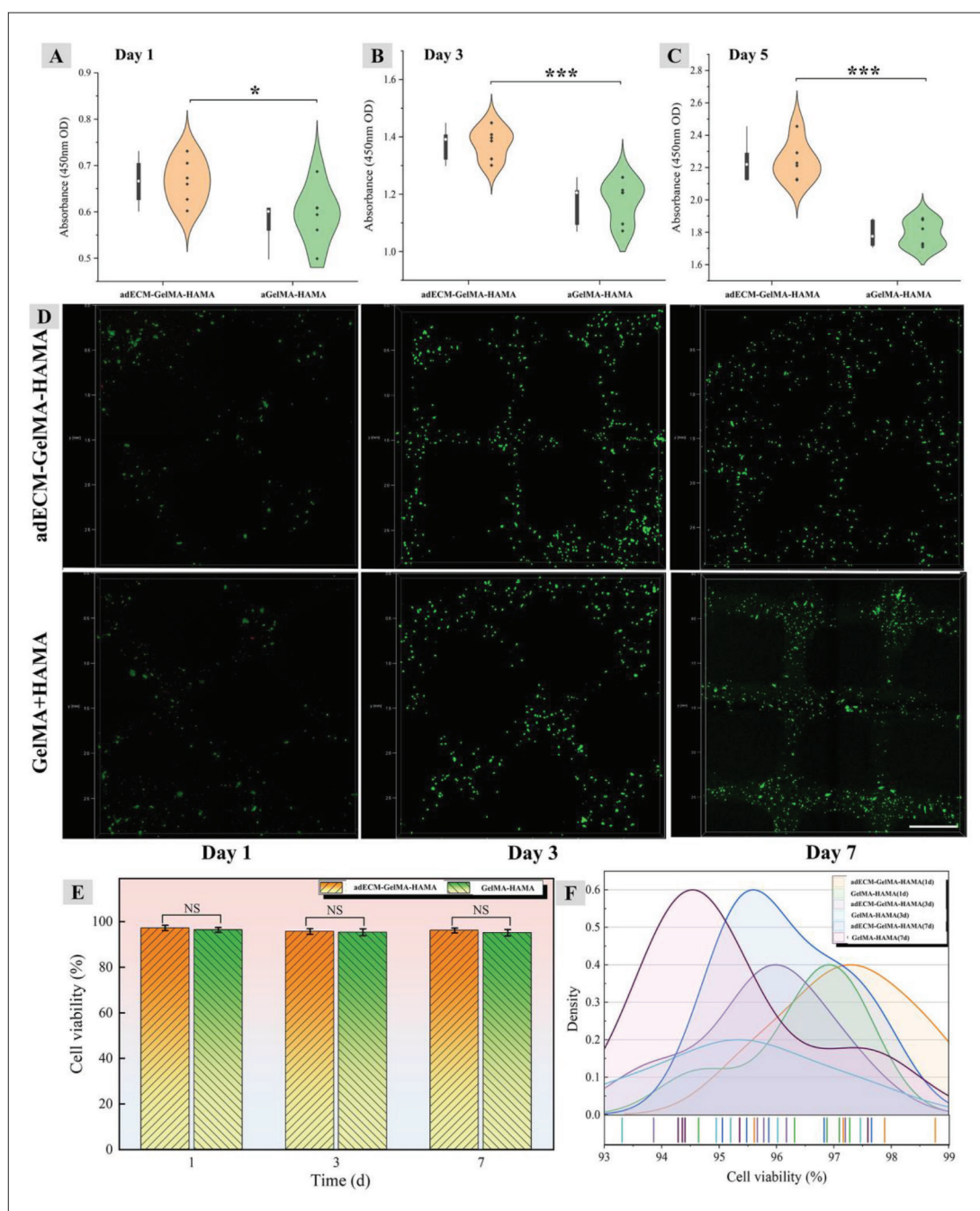


**Figure 7.** Biocompatibility of bioinks. (A–C) Optical density (OD, at 450 nm) values (CCK-8) of samples of ADSCs cultured in solutions of extract from adECM–GelMA–HAMA hydrogel for 1, 3, and 5 days. (D) Live/dead staining of cells within printed constructs after 1, 3, and 7 days. Scale bar: 100 μm. (E) Cell viability. (F) Distribution of cell viability. \* $p < 0.05$ , \*\* $p < 0.01$ , and \*\*\* $p < 0.001$ .

ADSC-laden adECM–GelMA–HAMA group ( $0.81\% \pm 1.14\%$ ) was remarkably reduced compared with that in the adECM–GelMA–HAMA, GelMA–HAMA, and blank control groups ( $6.67\% \pm 1.97\%$ ,  $16.65\% \pm 2.9\%$ , and  $29.42\% \pm 4.21\%$ , respectively) but was not remarkably different from that in the ADSC-laden GelMA–HAMA group ( $0.82\% \pm 1.52\%$ ; Figure 8C). Several studies have

confirmed that ADSCs can accelerate the wound-healing process<sup>[48–50]</sup>. In the early stage of wound healing, implanted MSCs recruit more endogenous cells through the paracrine effect for tissue remodeling. In the latter stage, exogenous cells gradually disappear, and endogenous cells gradually assume the responsibility of repair<sup>[51]</sup>. Another consideration is that ECM is involved in wound



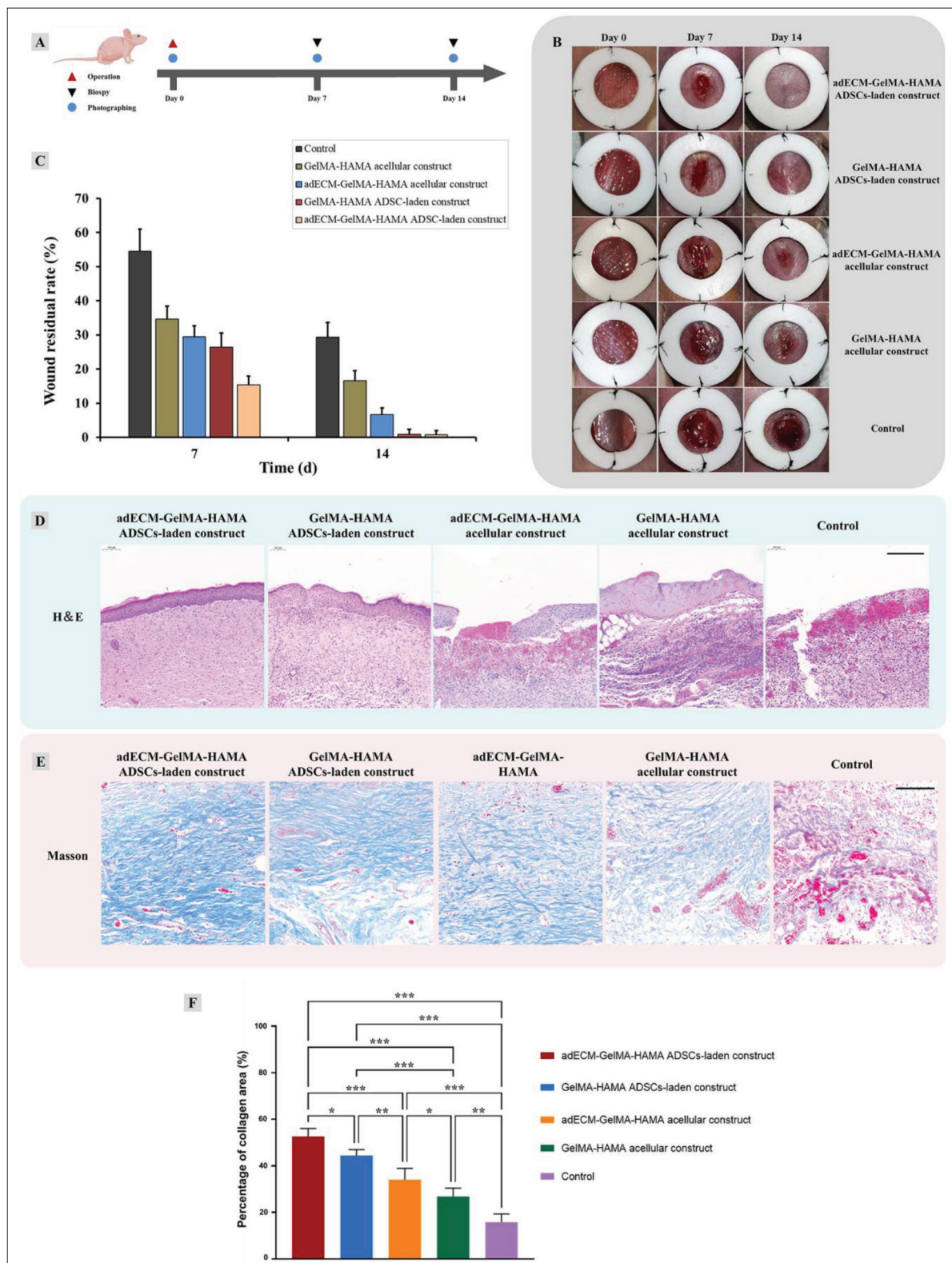


**Figure 8.** Ability of 3D-printed, ADSC-laden adECM-GelMA-HAMA construct to accelerate wound healing. (A) Protocol for an *in vivo* study. (B) Representative images of full-thickness skin excision wounds in different treatment groups over 14 days. (C) Quantitative analysis of wound closure in different groups. (D, E) Representative images of H&E-stained and Masson's trichrome-stained wound skin samples from different treatment groups after 14 days. Scale bar: 100  $\mu$ m. (F) Quantitative analysis of collagen regeneration in each group after 14 days. \* $p < 0.05$ , \*\* $p < 0.01$ , and \*\*\* $p < 0.001$ .

re-epithelialization through contact with keratinocytes or by affecting granulation tissue<sup>[52]</sup>.

### 3.8. Histopathological analysis of repaired skin

At day 14, the ADSC-laden adECM–GelMA–HAMA group was superior to the other groups for promoting the collagen III/I ratio, the deposition of collagen, and the expression of CD31. *In vivo* wound healing after treatment with different scaffolds was further evaluated histologically through H&E staining. On day 14 after implantation, the harvested tissues from the two ADSC-laden groups showed a well-organized epidermal structure and a well-distributed dermal structure with clear vascular and fibrous tissues and minimal inflammatory cell infiltration. We speculate that the limited inflammatory infiltration may be related to modulation of neutrophil, macrophage, and lymphocyte responses by MSC-secreted growth factors and cytokines<sup>[53]</sup>. In comparison, the epidermis was fractured in samples from the two groups treated with acellular scaffolds, and fibrous tissue hyperplasia was found in the dermis, especially in the GelMA–HAMA group. In the blank control group, no covered squamous epithelium was observed, and the dermis was dominated by inflammatory granulation tissue (Figure 8D). Porous scaffold structures have recently been shown to facilitate healthy fibroblast activity and inhibit myofibroblast activation<sup>[54]</sup>. The adipogenesis reported in previous studies was not observed here after implantation of ADSC-laden adECM–GelMA–HAMA scaffolds<sup>[55]</sup>.

Collagen synthesis and remodeling were evaluated using Masson's trichrome staining with quantitative analysis at 14 days after implantation. Collagen fibers in tissue samples from the ADSC-laden adECM–GelMA–HAMA and ADSC-laden GelMA–HAMA groups were denser and arranged in a more orderly fashion (Figure 8E) compared with those in the other groups. The collagen contents of samples from the ADSC-laden adECM–GelMA–HAMA and ADSC-laden GelMA–HAMA ( $52.62\% \pm 3.4\%$  and  $44.41\% \pm 2.57\%$ , respectively) were remarkably higher than those of samples from the adECM–GelMA–HAMA, GelMA–HAMA, and blank control groups ( $34.05\% \pm 4.85\%$ ,  $26.79\% \pm 3.61\%$ , and  $15.77\% \pm 3.55\%$ , respectively), with significant differences observed among the groups (Figure 8F).

The histological morphology of collagen I and III in each group was observed using Picrosirius red staining 14 days after implantation. Under polarized light microscopy, collagen I showed red or yellow birefringence, and collagen III showed green birefringence. Thus, the collagen content differed among the groups, which was consistent with Masson's trichrome staining, and the proportion of collagen I was higher than that of collagen

III in each group (Figure 9A). The ratio of collagen III to collagen I in the ADSC-laden adECM–GelMA–HAMA group ( $0.5 \pm 0.04$ ) was remarkably higher than those in the ADSC-laden GelMA–HAMA, adECM–GelMA–HAMA, GelMA–HAMA, and blank control groups ( $0.44 \pm 0.05$ ,  $0.19 \pm 0.05$ ,  $0.16 \pm 0.03$ , and  $0.08 \pm 0.03$ , respectively) (Figure 9B). These results indicate that adECM and ADSCs, in combination or individually, can increase the content of collagen type III and promote scarless wound healing. The collagen ratio reflects a dynamically evolving process, and during the maturation phase, the collagen fibers reorganize from type III collagen to type I collagen to complete the tissue remodeling<sup>[56,57]</sup>.

Angiogenesis and neovascularization are critical determinants during the wound-healing process<sup>[58]</sup>. Blood vessels provide oxygen and nutrients to maintain cell proliferation and structural remodeling<sup>[59]</sup>. The expression of endothelial cell biomarker CD31 was detected by immunohistochemical staining, and then wound neovascularization also was evaluated. Positive expression of CD31 was seen in all groups on day 14 after implantation (Figure 9C). The number of blood vessels in tissue samples from the ADSC-laden adECM–GelMA–HAMA group ( $60.5 \pm 6.14/\text{field}$ ) was remarkably higher than those from the ADSC-laden GelMA–HAMA, adECM–GelMA–HAMA, GelMA–HAMA, and blank control groups ( $50.38 \pm 4.32$ ,  $35.75 \pm 5.45$ ,  $29.38 \pm 3.77$ , and  $15.75 \pm 3.96/\text{field}$ ). Significant differences in the numbers of blood vessels were observed among all the groups (Figure 9D). These results indicate that adECM and ADSCs could promote angiogenesis during wound healing, whether acting together or alone.

These differences in wound neovascularization suggest that adECM and ADSCs alone or in combination can promote the formation of key physiological structures in wounds after implantation. ECM contributes to cell adhesion, tissue anchoring, cell signaling, and cell recruitment<sup>[60]</sup>. To date, the vast majority of natural or synthetic materials do not fully replicate all the natural features of ECM<sup>[37]</sup>. The adECM was chosen as the bioink component herein to provide a natural microenvironment similar to that of native adipose tissue for ADSCs, which may facilitate cell survival and retention of characteristics<sup>[61,62]</sup>. Upon placement in the wound microenvironment *in vivo*, ADSCs can continue to adapt to the wound microenvironment to function in promoting wound healing. Xu *et al.* injected adECM into the skin of mice and found that adECM increased dermal thickness, proliferating cell abundance, capillary density, and collagen types I and III expression<sup>[63]</sup>. This suggests that the microenvironment may play a determining role in the direction of tissue generation, independent

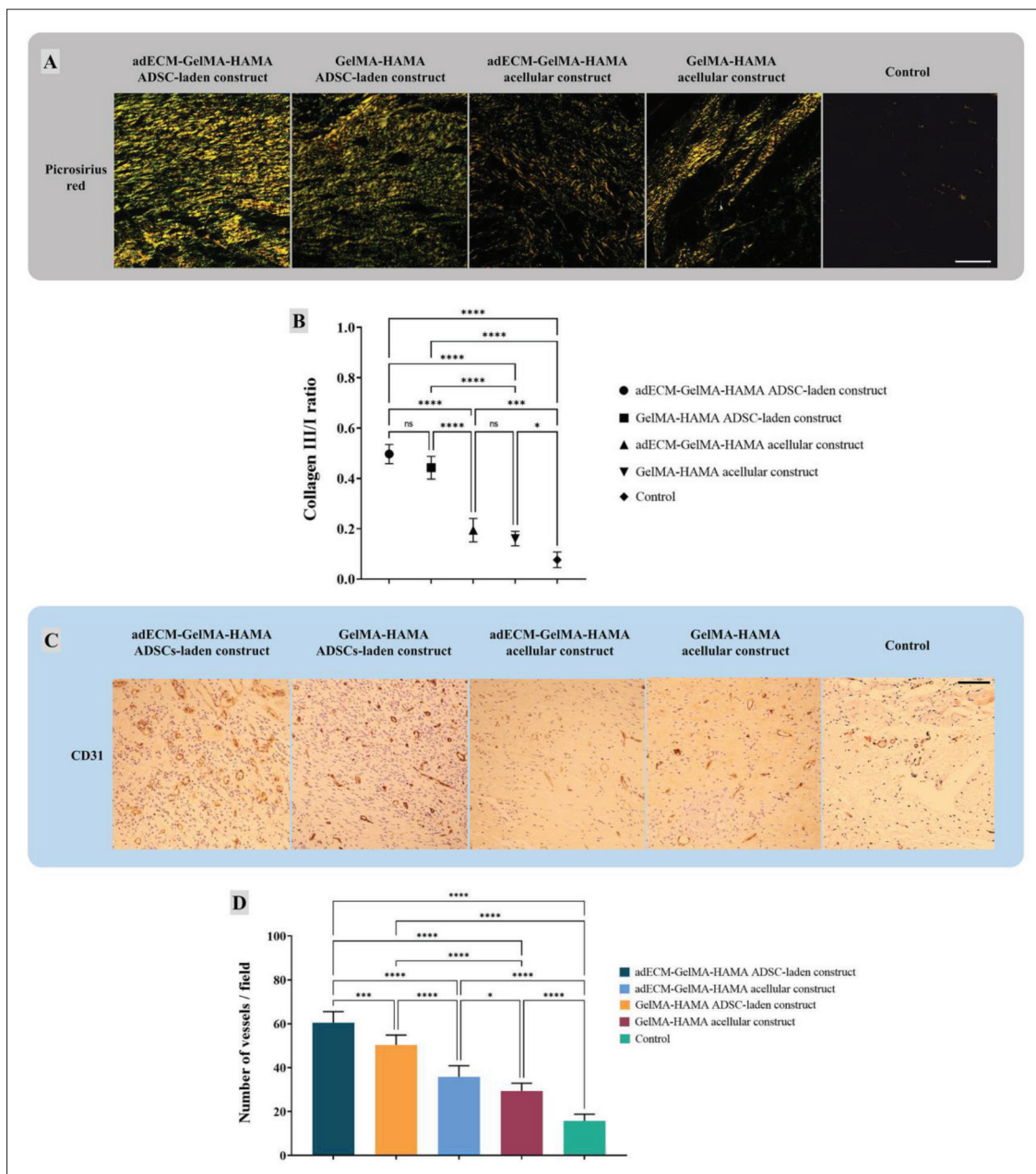


**Figure 9.** Ratio of collagen type III/collagen type I and angiogenesis within repaired skin tissue from each treatment group. (A) Representative images of Picrosirius red staining of repaired skin samples harvested after 14 days. Scale bar: 100  $\mu$ m. (B) Ratio of collagen type III (Col III) to collagen type I (Col I) in repaired skin samples from different treatment groups. (C) Distribution of blood vessels (CD31-positive area) identified by immunohistochemical staining in repaired skin samples harvested from different groups after 14 days. Scale bar: 100  $\mu$ m. (D) Quantitative analysis of CD31-positive (+) blood vessels in repaired skin samples harvested from different groups after 14 days. \* $p < 0.05$ , \*\* $p < 0.01$ , and \*\*\* $p < 0.001$ .

of the source tissue for MSCs or ECM. In the process of wound healing, this microenvironment may direct ADSCs to participate in tissue repair through different mechanisms, and further research is needed to elucidate these specific mechanisms<sup>[64]</sup>. This activity within the *in vivo* wound microenvironment supports the development of an “*in vitro* rapid fabrication + *in vivo* maturation in the

microenvironment” strategy adopted herein, which does not require *in vitro* preparation of a tissue-engineered material that completely matches the wound environment. This enables us to focus on maintaining the viability and identity of engrafted MSCs in the present study.

A limitation of this study is that ADSC survival, proliferation, and differentiation were not evaluated



after implantation. A specific microenvironment that provides complex communication is critical in regulating cell survival and differentiation<sup>[65]</sup>. Previous studies have confirmed that ADSCs can differentiate *in vivo* and adapt to microenvironmental conditions<sup>[66]</sup>. In skin regeneration studies, MSCs have been shown to differentiate into keratinocytes, dermal fibroblasts, and other skin components<sup>[67-70]</sup>. Therefore, our subsequent studies will focus on the possible cellular fates of ADSCs and the underlying regulatory mechanisms after implantation of the 3D-printed scaffolds.

## 5. Conclusion

The ADSC-laden 3D-printed scaffolds fabricated herein could address several clinical needs for treating major skin defects, such as sufficient material source, timely preparation, and efficacy. It is important to emphasize the rapid timeline for the preparation of these scaffolds, allowing sufficient material to be quickly obtained from human lipoaspirate for the fabrication of the clinically needed scaffolds. We found that the 3D-printed ADSC-laden adECM–GelMA–HAMA scaffold can accelerate wound healing in a mouse model by promoting angiogenesis and collagen synthesis, and this approach may consequently become a new treatment method for full-thickness skin defects.

## Acknowledgments

We thank the technical assistance of Dr. Jiachen Sun from the Department of Dermatology, Peking University Third Hospital.

## Funding

No fundings were received for this study.

## Conflict of interest

The authors declare no conflict of interest.

## Author contributions

**Conceptualization:** Minliang Chen, Dequan Zhang  
**Data curation:** Dequan Zhang, Huijuan Fu, Jinshi Zeng  
**Formal analysis:** Dequan Zhang  
**Investigation:** Dequan Zhang, Qiang Fu, Jinshi Zeng  
**Methodology:** Dequan Zhang  
**Resources:** Qiang Fu  
**Software:** Litao Jia  
**Supervision:** Minliang Chen  
**Validation:** Dequan Zhang, Huijuan Fu  
**Writing – original draft:** Dequan Zhang, Qiang Fu  
**Writing – review & editing:** Dequan Zhang, Minliang Chen

## Ethics approval and consent to participate

The use of clinical lipoaspirates was approved by the Ethics Committee of the PLA General Hospital (No. 2022KY135-KS001). All animal experiments were approved by the ethics committee of the Fourth Medical Center of PLA General Hospital (No. 2022-X18-03). Informed consent to participate in this study was obtained from the human subjects.

## Consent for publication

Written informed consent has been obtained from the human subjects involved in this study for publishing their data in the current paper.

## Availability of data

All data that support the findings of this study are included within the article.

## References

1. Fu X, 2020, Wound healing center establishment and new technology application in improving the wound healing quality in China. *Burns Trauma*, 8:tkaa038.  
<https://doi.org/10.1093/burnst/tkaa038>
2. Nussbaum SR, Carter MJ, Fife CE, *et al.*, 2018, An economic evaluation of the impact, cost, and Medicare policy implications of chronic nonhealing wounds. *Value Health*, 21(1):27–32.  
<https://doi.org/10.1016/j.jval.2017.07.007>
3. Wurzer P, Keil H, Branski LK, *et al.*, 2016, The use of skin substitutes and burn care—A survey. *J Surg Res*, 201(2): 293–298.  
<https://doi.org/10.1016/j.jss.2015.10.048>
4. Riha SM, Maarof M, Fauzi MB, 2021, Synergistic effect of biomaterial and stem cell for skin tissue engineering in cutaneous wound healing: A concise review. *Polymers (Basel)*, 13(10):1546.  
<https://doi.org/10.3390/polym13101546>
5. Stone RC, Stojadinovic O, Rosa AM, *et al.*, 2017, A bioengineered living cell construct activates an acute wound healing response in venous leg ulcers. *Sci Transl Med*, 9(371):eaaf8611.  
<https://doi.org/10.1126/scitranslmed.aaf8611>
6. Eudy M, Eudy CL, Roy S, 2021, Apligraf as an alternative to skin grafting in the pediatric population. *Cureus*, 13(7):e16226.  
<https://doi.org/10.7759/cureus.16226>
7. Dai C, Shih S, Khachemoune A, 2020, Skin substitutes for acute and chronic wound healing: An updated review. *J Dermatol Treat*, 31(6):639–648.  
<https://doi.org/10.1080/09546634.2018.1530443>



8. Niu C, Wang L, Ji D, *et al.*, 2022, Fabrication of SA/Gel/C scaffold with 3D bioprinting to generate micro-nano porosity structure for skin wound healing: A detailed animal in vivo study. *Cell Regen*, 11(1):10.  
<https://doi.org/10.1186/s13619-022-00113-y>
9. Pontiggia L, Van Hengel IA, Klar A, *et al.*, 2022, Bioprinting and plastic compression of large pigmented and vascularized human dermo-epidermal skin substitutes by means of a new robotic platform. *J Tissue Eng*, 13:20417314221088513.  
<https://doi.org/10.1177/20417314221088513>
10. Michael S, Sorg H, Peck CT, *et al.*, 2013, Tissue engineered skin substitutes created by laser-assisted bioprinting form skin-like structures in the dorsal skin fold chamber in mice. *PLoS One*, 8(3):e57741.  
<https://doi.org/10.1371/journal.pone.0057741>
11. Ng WL, Qi JTZ, Yeong WY, *et al.*, 2018, Proof-of-concept: 3D bioprinting of pigmented human skin constructs. *Biofabrication*, 10(2):025005.  
<https://doi.org/10.1088/1758-5090/aa9e1e>
12. Zhang Y, Enhejirigala, Yao B, *et al.*, 2021, Using bioprinting and spheroid culture to create a skin model with sweat glands and hair follicles. *Burns Trauma*, 9:tkab013.  
<https://doi.org/10.1093/burnst/tkab013>
13. Albanna M, Binder KW, Murphy SV, *et al.*, 2019, In situ bioprinting of autologous skin cells accelerates wound healing of extensive excisional full-thickness wounds. *Sci Rep*, 9(1):1856.  
<https://doi.org/10.1038/s41598-018-38366-w>
14. Jorgensen AM, Varkey M, Gorkun A, *et al.*, 2020, Bioprinted skin recapitulates normal collagen remodeling in full-thickness wounds. *Tissue Eng Part A*, 26(9-10):512–526.  
<https://doi.org/10.1089/ten.TEA.2019.0319>
15. He P, Zhao J, Zhang J, *et al.*, 2018, Bioprinting of skin constructs for wound healing. *Burns Trauma*, 6:5.  
<https://doi.org/10.1186/s41038-017-0104-x>
16. Raziyeve K, Kim Y, Zharkinbekov Z, *et al.*, 2021, Immunology of acute and chronic wound healing. *Biomolecules*, 11(5):700.  
<https://doi.org/10.3390/biom11050700>
17. Rodrigues M, Kosaric N, Bonham CA, *et al.*, 2019, Wound healing: A cellular perspective. *Physiol Rev*, 99(1):665–706.  
<https://doi.org/10.1152/physrev.00067.2017>
18. Shaik S, Wu X, Gimble JM, *et al.*, 2020, Non-toxic freezing media to retain the stem cell reserves in adipose tissues. *Cryobiology*, 96:137–144.  
<https://doi.org/10.1016/j.cryobiol.2020.07.005>
19. Chaudhuri O, Cooper-White J, Janmey PA, *et al.*, 2020, Effects of extracellular matrix viscoelasticity on cellular behaviour. *Nature*, 584(7822):535–546.  
<https://doi.org/10.1038/s41586-020-2612-2>
20. Frantz C, Stewart KM, Weaver VM, 2010, The extracellular matrix at a glance. *J Cell Sci*, 123(Pt 24):4195–4200.  
<https://doi.org/10.1242/jcs.023820>
21. Ventura RD, Padalhin AR, Park CM, *et al.*, 2019, Enhanced decellularization technique of porcine dermal ECM for tissue engineering applications. *Mater Sci Eng C Mater Biol Appl*, 104:109841.  
<https://doi.org/10.1016/j.msec.2019.109841>
22. Saldin LT, Cramer MC, Velankar SS, *et al.*, 2017, Extracellular matrix hydrogels from decellularized tissues: Structure and function. *Acta Biomater*. 49:1–15.  
<https://doi.org/10.1016/j.actbio.2016.11.068>
23. Panwar A, Tan LP, 2016, Current status of bioinks for micro-extrusion-based 3D bioprinting. *Molecules*, 21(6):685.  
<https://doi.org/10.3390/molecules21060685>
24. Yue K, Trujillo-de Santiago G, Alvarez MM, *et al.*, 2015, Synthesis, properties, and biomedical applications of gelatin methacryloyl (GelMA) hydrogels. *Biomaterials*, 73:254–271.  
<https://doi.org/10.1016/j.biomaterials.2015.08.045>
25. Zhai P, Peng X, Li B, *et al.*, 2020, The application of hyaluronic acid in bone regeneration. *Int J Biol Macromol*, 151:1224–1239.  
<https://doi.org/10.1016/j.ijbiomac.2019.10.169>
26. Dung TN, Han VD, Tien GN, *et al.*, 2021, Autologous adipose-derived stem cell (ADSC) transplantation in the management of chronic wounds. *Ann Burns Fire Disasters*, 34(4):343–350.
27. Tanios E, Ahmed TM, Shafik EA, *et al.*, 2021, Efficacy of adipose-derived stromal vascular fraction cells in the management of chronic ulcers: A randomized clinical trial. *Regen Med*, 16(11):975–988.  
<https://doi.org/10.2217/rme-2020-0207>
28. Zhang J, Liu Y, Chen Y, *et al.*, 2020, Adipose-derived stem cells: Current applications and future directions in the regeneration of multiple tissues. *Stem Cells Int*, 2020:8810813.  
<https://doi.org/10.1155/2020/8810813>
29. Sivan U, Jayakumar K, Krishnan LK, 2014, Constitution of fibrin-based niche for in vitro differentiation of adipose-derived mesenchymal stem cells to keratinocytes. *Biores Open Access*, 3(6):339–347.  
<https://doi.org/10.1089/biores.2014.0036>
30. Hutchings G, Janowicz K, Moncrieff L, *et al.*, 2020, The proliferation and differentiation of adipose-derived stem

- cells in neovascularization and angiogenesis. *Int J Mol Sci*, 21(11):3790.  
<https://doi.org/10.3390/ijms21113790>
31. Zhou ZQ, Chen Y, Chai M, *et al.*, 2019, Adipose extracellular matrix promotes skin wound healing by inducing the differentiation of adipose-derived stem cells into fibroblasts. *Int J Mol Med*, 43(2):890–900.  
<https://doi.org/10.3892/ijmm.2018.4006>
  32. Lee DE, Ayoub N, Agrawal DK, 2016, Mesenchymal stem cells and cutaneous wound healing: Novel methods to increase cell delivery and therapeutic efficacy. *Stem Cell Res Ther*, 7:37.  
<https://doi.org/10.1186/s13287-016-0303-6>
  33. Roshangar L, Rad JS, Kheirjou R, *et al.*, 2021, Using 3D-bioprinting scaffold loaded with adipose-derived stem cells to burns wound healing. *J Tissue Eng Regen Med*, 15(6):546–555.  
<https://doi.org/10.1002/term.3194>
  34. Wu Y, Liang T, Hu Y, *et al.*, 2021, 3D bioprinting of integral ADSCs-NO hydrogel scaffolds to promote severe burn wound healing. *Regen Biomater*, 8(3):rbab014.  
<https://doi.org/10.1093/rb/rbab014>
  35. Flynn LE, 2010, The use of decellularized adipose tissue to provide an inductive microenvironment for the adipogenic differentiation of human adipose-derived stem cells. *Biomaterials*, 31(17):4715–4724.  
<https://doi.org/10.1016/j.biomaterials.2010.02.046>
  36. Crapo PM, Gilbert TW, Badylak SF, 2011, An overview of tissue and whole organ decellularization processes. *Biomaterials*, 32(12):3233–3243.  
<https://doi.org/10.1016/j.biomaterials.2011.01.057>
  37. Aamodt JM, Grainger DW, 2016, Extracellular matrix-based biomaterial scaffolds and the host response. *Biomaterials*, 86:68–82.  
<https://doi.org/10.1016/j.biomaterials.2016.02.003>
  38. Pati F, Jang J, Ha DH, *et al.*, 2014, Printing three-dimensional tissue analogues with decellularized extracellular matrix bioink. *Nat Commun*, 5:3935.  
<https://doi.org/10.1038/ncomms4935>
  39. Paxton N, Smolan W, Bock T, *et al.*, 2017, Proposal to assess printability of bioinks for extrusion-based bioprinting and evaluation of rheological properties governing bioprintability. *Biofabrication*, 9(4):044107.  
<https://doi.org/10.1088/1758-5090/aa8dd8>
  40. Holzl K, Lin S, Tytgat L, *et al.*, 2016, Bioink properties before, during and after 3D bioprinting. *Biofabrication*, 8(3):032002.  
<https://doi.org/10.1088/1758-5090/8/3/032002>
  41. Somasekharan LT, Kasoju N, Raju R, *et al.*, 2020, Formulation and characterization of alginate dialdehyde, gelatin, and platelet-rich plasma-based bioink for bioprinting applications. *Bioengineering (Basel)*, 7(3):108.  
<https://doi.org/10.3390/bioengineering7030108>
  42. Aboomeirah AA, Sarhan WA, Khalil EA, *et al.*, 2022, Wet electrospun nanofibers-fortified gelatin/alginate-based nanocomposite as a single-dose biomimicking skin substitute. *ACS Appl Bio Mater*, 5(8):3678–3694.  
<https://doi.org/10.1021/acsabm.2c00147>
  43. Lutzweiler G, Barthes J, Koenig G, *et al.*, 2019, Modulation of cellular colonization of porous polyurethane scaffolds via the control of pore interconnection size and nanoscale surface modifications. *ACS Appl Mater Interfaces*, 11(22):19819–19829.  
<https://doi.org/10.1021/acsami.9b04625>
  44. Ng WL, Lee JM, Zhou M, *et al.*, 2020, Vat polymerization-based bioprinting-process, materials, applications and regulatory challenges. *Biofabrication*, 12(2):022001.  
<https://doi.org/10.1088/1758-5090/ab6034>
  45. Ng WL, Huang X, Shkolnikov V, *et al.*, 2022, Controlling droplet impact velocity and droplet volume: Key factors to achieving high cell viability in sub-nanoliter droplet-based bioprinting. *Int J Bioprint*, 8(1):424.  
<https://doi.org/10.18063/ijb.v8i1.424>
  46. Jiang T, Munguia-Lopez JG, Flores-Torres S, *et al.*, 2019, Extrusion bioprinting of soft materials: An emerging technique for biological model fabrication. *Appl Phys Rev*, 6:011310.  
<https://doi.org/10.1063/1.5059393>
  47. Barros NR, Kim HJ, Goudie MJ, *et al.*, 2021, Biofabrication of endothelial cell, dermal fibroblast, and multilayered keratinocyte layers for skin tissue engineering. *Biofabrication*, 13(3).  
<https://doi.org/10.1088/1758-5090/aba503>
  48. Almalki SG, 2022, Adipose-derived mesenchymal stem cells and wound healing: Potential clinical applications in wound repair. *Saudi Med J*, 43(10):1075–1086.  
<https://doi.org/10.15537/smj.2022.43.10.20220522>
  49. Zhou L, Wang H, Yao S, *et al.*, 2022, Efficacy of human adipose derived mesenchymal stem cells in promoting skin wound healing. *J Healthc Eng*, 2022:6590025.  
<https://doi.org/10.1155/2022/6590025>
  50. Huayllani MT, Sarabia-Estrada R, Restrepo DJ, *et al.*, 2020, Adipose-derived stem cells in wound healing of full-thickness skin defects: A review of the literature. *J Plast Surg Hand Surg*, 54(5):263–279.  
<https://doi.org/10.1080/2000656X.2020.1767116>

51. Wang N, Liu H, Li X, *et al.*, 2017, Activities of MSCs derived from transgenic mice seeded on ADM scaffolds in wound healing and assessment by advanced optical techniques. *Cell Physiol Biochem*, 42(2):623–639.  
<https://doi.org/10.1159/000477872>
52. Rousselle P, Montmasson M, Garnier C, 2019, Extracellular matrix contribution to skin wound re-epithelialization. *Matrix Biol*, 75–76:12–26.  
<https://doi.org/10.1016/j.matbio.2018.01.002>
53. Li ZJ, Wang LQ, Li YZ, *et al.*, 2021, Application of adipose-derived stem cells in treating fibrosis. *World J Stem Cells*, 13(11):1747–1761.  
<https://doi.org/10.4252/wjsc.v13.i11.1747>
54. Ibañez RIR, do Amaral RJFC, Reis RL, *et al.*, 2021, 3D-printed gelatin methacrylate scaffolds with controlled architecture and stiffness modulate the fibroblast phenotype towards dermal regeneration. *Polymers (Basel)*, 13(15):2510.  
<https://doi.org/10.3390/polym13152510>
55. Pati F, Ha D-H, Jang J, *et al.*, 2015, Biomimetic 3D tissue printing for soft tissue regeneration. *Biomaterials*, 62: 164–175.  
<https://doi.org/10.1016/j.biomaterials.2015.05.043>
56. Baron JM, Glatz M, Proksch E, 2020, Optimal support of wound healing: New insights. *Dermatology*, 236(6):593–600.  
<https://doi.org/10.1159/000505291>
57. Leavitt T, Hu MS, Marshall CD, *et al.*, 2016, Scarless wound healing: Finding the right cells and signals. *Cell Tissue Res*, 365(3):483–493.  
<https://doi.org/10.1007/s00441-016-2424-8>
58. Sorg H, Tilkorn DJ, Mirastschijski U, *et al.*, 2018, Panta rhei: Neovascularization, angiogenesis and nutritive perfusion in wound healing. *Eur Surg Res*, 59(3–4):232–241.  
<https://doi.org/10.1159/000492410>
59. DiPietro LA, 2016, Angiogenesis and wound repair: When enough is enough. *J Leukoc Biol*, 100(5):979–984.  
<https://doi.org/10.1189/jlb.4MR0316-102R>
60. Diller RB, Tabor AJ, 2022, The role of the extracellular matrix (ECM) in wound healing: A review. *Biomimetics (Basel)*, 7(3):87.  
<https://doi.org/10.3390/biomimetics7030087>
61. Moffat D, Ye K, Jin S, 2022, Decellularization for the retention of tissue niches. *J Tissue Eng*, 13:20417314221101151.  
<https://doi.org/10.1177/20417314221101151>
62. Guilak F, Cohen DM, Estes BT, *et al.*, 2009, Control of stem cell fate by physical interactions with the extracellular matrix. *Cell Stem Cell*, 5(1):17–26.  
<https://doi.org/10.1016/j.stem.2009.06.016>
63. Xu Y, Deng M, Cai Y, *et al.*, 2020, Cell-free fat extract increases dermal thickness by enhancing angiogenesis and extracellular matrix production in nude mice. *Aesthet Surg J*, 40(8):904–913.  
<https://doi.org/10.1093/asj/sjz306>
64. Mazini L, Rochette L, Admou B, *et al.*, 2020, Hopes and limits of adipose-derived stem cells (ADSCs) and mesenchymal stem cells (MSCs) in wound healing. *Int J Mol Sci*, 21(4):1306.  
<https://doi.org/10.3390/ijms21041306>
65. Zhang P, Zhang C, Li J, *et al.*, 2019, The physical microenvironment of hematopoietic stem cells and its emerging roles in engineering applications. *Stem Cell Res Ther*, 10(1):327.  
<https://doi.org/10.1186/s13287-019-1422-7>
66. Zhou X, Wang J, Huang X, *et al.*, 2018, Injectable decellularized nucleus pulposus-based cell delivery system for differentiation of adipose-derived stem cells and nucleus pulposus regeneration. *Acta Biomater*, 81:115–128.  
<https://doi.org/10.1016/j.actbio.2018.09.044>
67. Xiao Y, Peng J, Liu Q, *et al.*, 2020, Ultrasmall CuS@BSA nanoparticles with mild photothermal conversion synergistically induce MSCs-differentiated fibroblast and improve skin regeneration. *Theranostics*, 10(4):1500–1513.  
<https://doi.org/10.7150/thno.39471>
68. An R, Zhang Y, Qiao Y, *et al.*, 2020, Adipose stem cells isolated from diabetic mice improve cutaneous wound healing in streptozotocin-induced diabetic mice. *Stem Cell Res Ther*, 11(1):120.  
<https://doi.org/10.1186/s13287-020-01621-x>
69. Liubaviciute A, Kaseta V, Vaitkuvienė A, *et al.*, 2018, Regenerative potential of partially differentiated mesenchymal stromal cells in a mouse model of a full-thickness skin wound. *Excl J*, 17:871–888.  
<https://doi.org/10.17179/excli2018-1504>
70. Dos Santos JF, Borcari NR, Silva Araujo, *et al.*, 2019, Mesenchymal stem cells differentiate into keratinocytes and express epidermal kallikreins: Towards an in vitro model of human epidermis. *J Cell Biochem*, 120(8):13141–13155.  
<https://doi.org/10.1002/jcb.28589>